REGULAR PAPER

Optimization of Co additive amount to improve thermoelectric properties of β-FeSi$_2$

View the article online for updates and enhancements.

REGULAR PAPER

Optimization of Co additive amount to improve thermoelectric properties of β-FeSi$_2$

Sopheap Sam[1], Hiroshi Nakatsugawa[1*], and Yoichi Okamoto[2]

[1]Yokohama National University, Japan
[2]National Defense Academy, Japan

*E-mail: nakatsugawa-hiroshi-dx@ynu.ac.jp

The present manuscript deals with the synthesis of pure and Co-doped β-FeSi$_2$ by the conventional arc-melting method and the investigation of the effect of Co-dopant on the structural, electrical, and thermoelectric properties of β-Fe$_{1-x}$Co$_x$Si$_2$ ($0 \leqslant x \leqslant 0.06$) from 300 to 800 K. The electrical resistivity decreases with increasing Co-doping due to the increase in carrier concentration. The Seebeck coefficient of all Co-doping samples ($0.005 \leqslant x \leqslant 0.06$) is higher and more stable than that of $x = 0$ due to the absence of the bipolar effect. Therefore, the maximum power factor is around 900 μWm^{-1}K^{-2} obtained in $x = 0.03$ from 720 to 800 K. The thermal conductivity also slightly decreases with increasing x. As a result, the optimum doping level is achieved in $x = 0.03$ with the carrier density around $1.2(4) \times 10^{20}$ cm^{-3} and mobility for 3.5(6) cm^2 V^{-1} s^{-1}, where the highest ZT is 0.099. © 2022 The Japan Society of Applied Physics

1. Introduction

Optimization of energy consumption is one of the key solutions to sustain the utilization of energy for future generations. Looking at the statistical estimation of energy used in various kinds of industries such as nuclear power plants, thermal power, waste incinerator, natural gas power plant, and automobile, and energy consumed by humans supplied from oil, gas, coal, etc, around more than 2/3 of primary energy is lost in form of waste heat, while only approximately 1/3 of that is the useful energy. To optimize the utilization of energy, many technological solutions have been proposed for its appropriate problems. Among various solutions, the thermoelectric (TE) system is considered the promising technique to harvest and directly convert the waste heat into electrical energy using the Seebeck effect without any moving part, no exhaust gas or mechanical pollution to the environment and no maintenance required.[1–4] To get a high conversion efficiency, it is required to develop semiconducting materials having high TE performance (ZT). The ZT of TE materials is theoretically equal to $S^2T/(\rho\kappa_{\text{total}})$, where S, T, ρ, and κ_{total}, are the Seebeck coefficient, absolute temperature, electrical resistivity, and thermal conductivity, respectively. However, the TE materials limit the application of TE devices because the materials having acceptable conversion efficiency are rare and high-priced.[5] Therefore, researchers are trying to develop abundant and low-cost materials to boost TE conversion efficiency; therefore, the return on investment of TE systems will be considered by industry sectors.

Among various TE materials, β-FeSi$_2$, which has an orthorhombic crystalline structure with a *Cmce* space group, is considered a potential candidate for high-temperature application due to its environmental friendliness, good thermal stability, strong oxidation resistance, and low cost.[6–9]

However, the ZT of non-doped β-FeSi$_2$ is still not high enough which limits its application in TE devices.[10,11] The low ZT is because of the decrease in $|S|$ as temperature increases due to the bipolar diffusion effect, and the high ρ due to low carrier concentration (n_H). The bipolar effect often occurs in narrow band gap semiconductors at low n_H.[12–21]

The effective mass of electrons is heavier than that of holes ($m_e^* > m_h^*$); therefore, the mobility of holes is higher than that of electrons ($\mu_e^* < \mu_h^*$). In addition, non-doped β-FeSi$_2$ has a narrow band gap of about 0.73 eV,[22] which is sensitive to the bipolar effect. As a result, the $|S|$ decreases with increasing temperature because of the presence of the bipolar effect. As $|S|$ decreases, the power factor (PF) or the ZT also gets a negative impact. Therefore, the reduction in bipolar effect and decrease in electrical resistivity can be simultaneously achieved by increasing n_H with larger valence electrons element doping techniques. Therefore, many previous works were conducted by doping with various impurities in order to enhance the n_H. Ohtaki et al. investigated the effect of Cu, Zn, Nb, Ag, and Sb doping on the crystalline β-FeSi$_2$ and showed that the microstructures of the samples were significantly varied by those dopants leading to obtaining $ZT_{\text{max}} = 0.026$ at 873 K.[23] In addition, Tani and Kido investigated the effect of Co substitution on Fe$_{1-x}$Co$_x$Si$_2$ ($x = 0.01$, 0.03, 0.05 and 0.1). The highest TE performance from their studies was achieved for $x = 0.05$ with maximum $ZT = 0.25$ at 940 K.[24] Kim et al. reported that the $ZT_{\text{max}} = 0.11$ at 845 K of β-FeSi$_2$ was achieved by co-doping: Co and Ge.[25] Ur reported that the maximum ZT in their study was 0.06 at 600 K from n-type Fe$_{0.98}$Co$_{0.02}$Si$_2$ fabricated by mechanical alloying and then by vacuum hot-pressing process.[26] Ito et al. found that by adding a small amount of SiO$_2$ to the β-Fe$_{0.98}$Co$_{0.02}$Si$_2$, the thermal conductivity was significantly reduced, and the resistivity was slightly increased, where the Seebeck coefficient was enhanced at low temperature. The high ZT from their study was about 0.08 at 655 K with the addition of 4% mass of SiO$_2$.[4] Redzuan et al. fabricated Fe$_{28.49}$Co$_{0.59}$Si$_{70.5}$ and followed by a hot-pressed sintering method. The annealing time and temperature were the main variables for their studies. They reported that the highest ZT was 0.085 for an annealing time of 4 h at a temperature of 1073 K.[27] Le Tonquesse et al. investigated the thermoelectric properties of β-FeSi$_2$ and β-Fe$_{0.93}$Co$_{0.07}$Si$_2$ fabricated by magnesiothermic process and followed by spark plasma sintering techniques. After the magnesiothermic process, the grain size of the sample was ranging from 30 to 40 nm. They reported that the improved $ZT = 0.18$ at 773 K was achieved from β-Fe$_{0.93}$Co$_{0.07}$Si$_2$.[28]

On the other hand, Dabrowski et al. investigated various kinds of dopants such as Mn, Co, Al, and P. They reported that the best dopant was Co with the highest $ZT = 0.15$ for $Fe_{0.97}Co_{0.03}Si_2$ at 773 K, resulting from significant improvement of the Seebeck coefficient and electrical conductivity.[11] According to a series of previous research, Co is considered the effective element for enhancing TE performance β-FeSi$_2$. In addition, based on the theoretical calculation, it was reported that the optimum carrier concentration for improving TE properties of β-FeSi$_2$ composites should be within 1×10^{20} to 2×10^{21} cm^{-3}.[8] However, the optimum Co addition amount (x) and the optimum carrier concentration (n_H) to enhance the TE properties of β-FeSi$_2$ have not yet been investigated.

In this present work, the study of the bipolar effect, the optimum doping concentration of Co (x), and the optimum carrier concentration (n_H) on the thermoelectric properties of β-Fe$_{1-x}$Co$_x$Si$_2$ fabricated by conventional arc-melting are investigated. In Fe$_{1-x}$Co$_x$Si$_2$ with $0 \leqslant x \leqslant 0.10$, we can clearly observe the significant effect of Co-dopant on the phase transition and its TE properties over the measured temperature range from 300 to 800 K.

2. Experimental methods

The raw materials of Fe (grain 99.9% up), Si (grain 99.999%), and Co (powder 99% up) were weighed according to their atomic composition Fe$_x$Co$_{1-x}$Si$_2$ where $0 \leqslant x \leqslant 0.10$. The mixtures of raw materials were arc-melted under vacuum conditions 10^{-5} torr in an Ar atmosphere. Titanium (Ti) 10 g was also set and initially melted in order to absorb the residual oxygen. The ingots were flipped and remelted 3 times to get a uniform material distribution. After arc melting, the ingots were cut into pieces (size $W \times L \times T = 7$ mm $\times$ 7 mm $\times$ 1.5 mm) using numerical control (NC) wire cutting machine. The samples were then polished to remove the oxidized surfaces before vacuum sealing in a silica quartz tube. The samples cut from the ingot were in α and ε phases; therefore, to get a single β phase, they need to be heat-treated at 1423 K for 3 h and followed by annealing at 1113 K for 20 h. The heat treatment and annealing conditions followed Ref. 23.

The crystal structure identification was calculated by Rietveld analysis (RIETAN-FP program) from the XRD data measured by CuKα diffractometer (SmartLab, Rigaku). The relative density was measured at room temperature by using the Archimedes method. The microstructure was visualized by using a scanning electron microscope (SEM, VE-8800). The resistivity (ρ), and the Seebeck coefficient (S) were measured by ResiTest8300 apparatus at the temperature range from 300 to 395 K and homemade apparatus at the temperature range from 400 to 800 K. The Hall parameters such as carrier concentration and mobility were also measured by ResiTest8300 at room temperature. The total thermal conductivity (κ_{total}) was measured by a power efficiency measurement system (PEM-2). The ZT can be calculated from T, S, ρ, and κ_{total}.

3. Results and discussion

The results of X-ray diffraction (XRD) analysis of Fe$_{1-x}$Co$_x$Si$_2$ are shown in Fig. 1. The samples grown in β-phase can be obtained in $0 \leqslant x \leqslant 0.06$ samples; however,

the small amount of ε-phase still remains at $2\theta \approx 45.2°$ as shown in the inset of Fig. 1. In addition, the presence of the (312) Bragg peak of an α-phase (metallic phase) is found in $0.07 \leqslant x \leqslant 0.10$ samples at $2\theta \approx 37.6°$, while that of the β-phase of $0 \leqslant x \leqslant 0.06$ samples is at $2\theta \approx 37.3°$. Figure 2 shows the SEM images of $0 \leqslant x \leqslant 0.10$. As shown in Fig. 2 (a), for $x = 0$ before heat treatment, the sample consists of a metallic phase ($\alpha + \varepsilon$, where the α-phase is the dark grain, while the ε-phase is the bright grain) which is in agreement with the study of Dąbrowski et al.[11] The white inclusions, which look like the glass reflection, are not microstructures but surface dust that is certainly coming from contamination with the polishing substrate during the early polishing process. After heat treatment, the bright grains are disappeared; therefore, the α and ε-phases are transformed into a β-phase for $0 \leqslant x \leqslant 0.06$ as shown in Figs. 2(b)–2(h). Since the amount of ε-phase contained in the $x \leqslant 0.07$ samples is probably too small as can be identified by a small peak in XRD powder measurement in Fig. 1, it is hard to visualize by using SEM measurement. However, Fig. 2(i) shows the existence of α-phase in the $x = 0.07$ sample as can be seen in the slightly dark area of the image. As shown in Fig. 2(j), the ε-phase can be identified in the $x = 0.10$ sample because the diffraction peak at $2\theta \approx 45.2°$ of this sample is higher than that of $0 \leqslant x \leqslant 0.07$ samples. This confirms that the results of SEM images verify with XRD peak in Fig. 1. Dąbrowski et al. reported that after the heat treatment, the presence of $\varepsilon + \beta$-phase in the $x = 0.03$ sample can be identified with the SEM image. This is probably because the amount of ε-phase contained in their samples is higher than that of our samples. It is considered that the presence of a higher amount of ε-phase in their sample is probably due to the higher heat treatment temperature (1123 K) and the shorter time (only 10 h). On the other hand, Kojima et al. reported that they were able to achieve a single β-phase up to $x \leqslant 0.116$.[29] Since the annealing time and temperature of the current study and that of Kojima et al. are the same, the difference between phase transition dependent on Co concentration should be caused by the purity of raw materials. They were using iron (purity, 99%) and silicon (purity, 98%), which has a lower purity than our materials as mentioned in the experimental section. Therefore, it is considered that the formation of the β-phase is so sensitive to the purity of the materials. In addition, as can be seen in Fig. 2(a), some pores were formed before heat treatment. The formation of those pores is probably due to the contraction of a heterogeneous solid (ε-FeSi + α-FeSi$_2$) during the fast cooling of the water-cooled copper plate in the arc melting process. In addition, the size of the pores of samples after heat treatment as shown in Figs. 2(b)–2(i) is relatively larger than those of the sample before heat treatment as shown in Fig. 2(a). The increase in their sizes occurred during the formation of the semiconducting β-phase when the volume occupied by β-FeSi$_2$ differs from the volume occupied by ε-FeSi and α-FeSi$_2$ (ε-FeSi + α-FeSi$_2 \rightarrow \beta$-FeSi$_2$). The correlation between the enlargement in pore size and the decrease in thermal conductivity is not clear at this time and is an issue for the future. Moreover, there is no remarkable crack formed after annealing. In addition, as shown in Table I, the relative densities of samples after the heat treatment range from 96.9 (1)% to 98.5(2)%. Such values agree with the samples
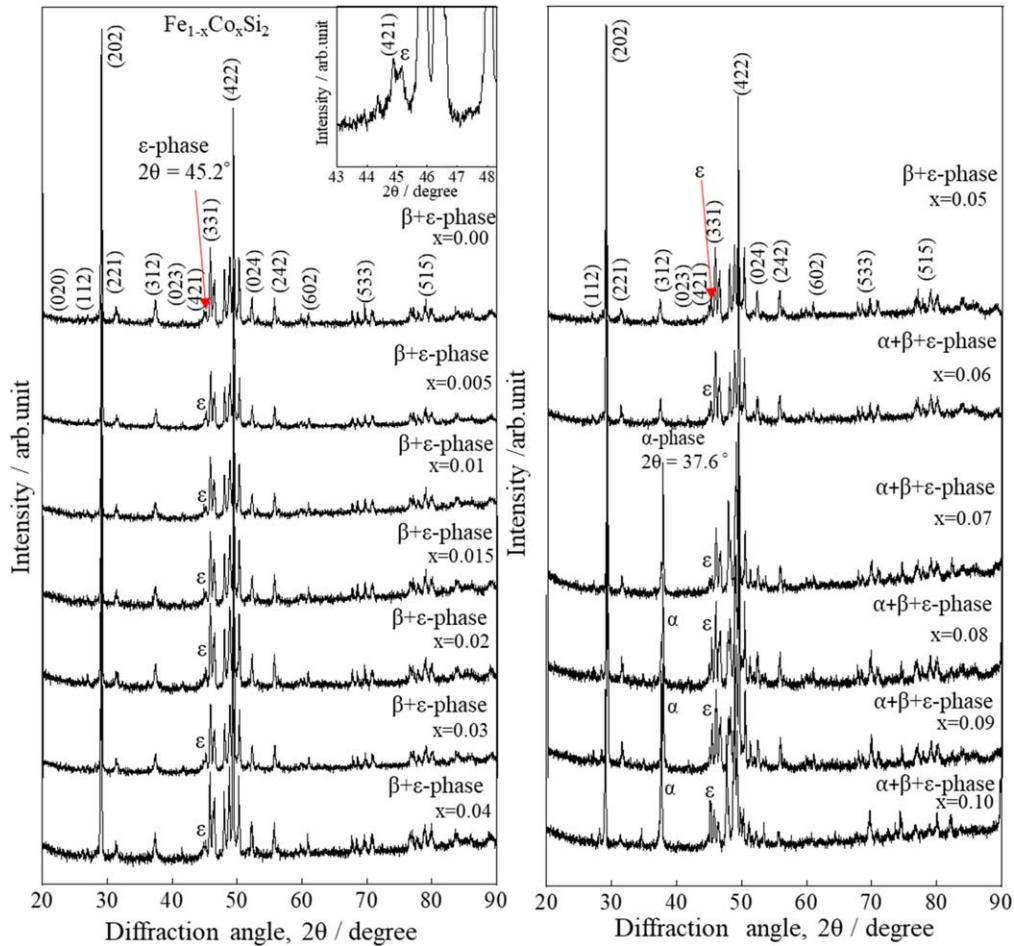
Fig. 1.   (Color online) X-ray diffraction patterns of $Fe_{1-x}Co_xSi_2$ ($0 \leqslant x \leqslant 0.10$) at room temperature, where the indexed peaks are the peaks of β-phase and the inset shows a peak of ε-phase at $2\theta = 45.2°$.

fabricated by hot-pressing (HP),[30] but are relatively higher than those fabricated by spark plasma sintering (SPS),[30,31] and pulse plasma sintering (PPS).[11,32] This indicates that the high relative density can be obtained by samples prepared by arc melting and annealing methods; therefore, the decrease in electrical resistivity can be achieved, resulting in the enhancement of thermoelectric performance.

Since the TE performance of the metallic phase is theoretically quite low due to the decrease in the Seebeck coefficient ($S = -\Delta V/\Delta T$) and high thermal conductivity (κ), the characterization of TE properties was performed only for $0 \leqslant x \leqslant 0.06$ samples. The three-dimensional crystal structure of β-FeSi$_2$ can be seen in Fig. 3. Each of the Fe1 and Fe2 sites is bounded in an 8-coordinate geometry to four Si1 and four Si2 sites with a spread of Fe–Si bond distances ranging from 2.361(5) to 2.402(6) Å and from 2.282(5) to 2.415(4) Å, respectively, as shown in Table II.

Figure 4 shows the Rietveld analysis where the red, green, and blue curves represent the experimental, calculated, and different data, respectively. Based on primal indexed peaks except for a small peak at $2\theta = 45.2°$, it can be clearly confirmed that the sample was grown in a β-phase after heat treatment at 1423 K for 3 h and annealing at 1113 K for 20 h, verifying the SEM images in Figs. 2(b)–2(h). At $2\theta = 45.2°$, it is considered that a small amount of impurity, which is the ε-phase, probably remains, but it should not cause any significant effect on the TE properties. The crystal structure

analysis was performed using an orthorhombic structure with a *Cmce* space group. The crystal structure parameters refinement by the Rietveld analysis using the RIETAN-FP program are summarized in Table II. The occupancy rate of Fe1 and Fe2 sites was set to 1-x while that of Co1 and Co2 was set to x for $0 \leqslant x \leqslant 0.10$. The isotropic atomic displacement parameters B were fixed to 1.0 Å^2 for both the Fe site and Si site. The Bragg peak profiles were fitted using a split pseudo-Voigt function. As shown in Fig. 5(a), the lattice constant a increases with increasing x, while b and c are independent of x. This result agrees with Kojima et al.,[29] indicating that Co atoms are dissolved in a solid solution of FeSi$_2$ up to $x = 0.06$. The x dependence of Si–Fe distances is shown in Fig. 5(b). As x increases, the Si1–Fe1 and the Si1–Fe2 distances tend to slightly increase, having the same tendency as the lattice constant a. This suggests that the Si1–Fe1 and the Si1–Fe2 bonds are probably oriented in the same direction with lattice constant a. On the other hand, the Si2–Fe1 and the Si2–Fe2 distances are constant with increasing x. In addition, the x dependence of Fe–Si–Fe angles is shown in Fig. 5(c). As x increases, the angles of Fe1–Si1–Fe1 and Fe1–Si2–Fe1 tend to increase, while those of Fe2–Si1–Fe2 and Fe2–Si2–Fe2 tend to decrease. This result suggests that both Fe1 and Fe2 site is slightly varied as x increases. It is considered that there is no preferential site for Co in either one of the Fe1 or Fe2 sites. In other words, the Co populations equally participated in both Fe1 and Fe2 sites
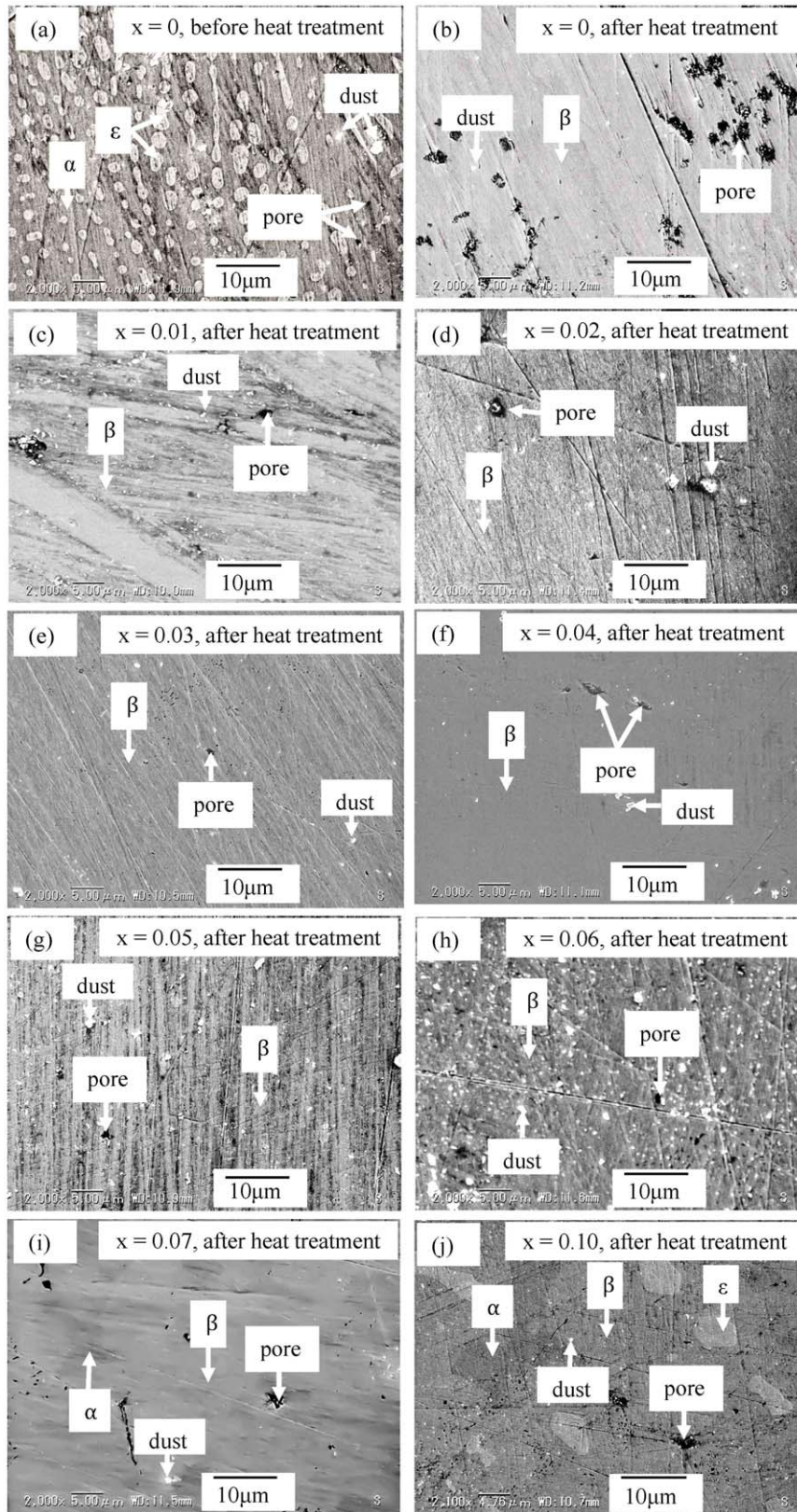
Fig. 2. (Color online) SEM image of $Fe_{1-x}Co_xSi_2$ ($0 \leqslant x \leqslant 0.10$), (a) of $x = 0$ before heat treatment, (b)–(j) of $0 \leqslant x \leqslant 0.10$ after heat treatment.

in the β-$Fe_{1-x}Co_xSi_2$ system which is in agreement with Ref. 33. Importantly, as shown in Fig. 5(d), the reliability factor R_{wp} of the weighted diffraction pattern is approximately stable for $0.0 \leqslant x \leqslant 0.06$ indicating a good fit between observed and computed intensities, and the presence of a single β-phase with a trace of ε-FeSi. However, it significantly increases at $x \geqslant 0.07$ probably due to the presence of a

second phase which is the α-phase, verifying the XRD patterns in Fig. 1.

The carrier concentration (n_H), carrier mobility (μ_H), absolute Seebeck coefficient ($|S|$), electrical resistivity (ρ), and total thermal conductivity (κ) of β-$Fe_{1-x}Co_xSi_2$ ($0 \leqslant x \leqslant 0.06$) at room temperature are summarized in Table I. The n_H of non-doped β-$FeSi_2$ is about

Table I. Lorenz number (L_O), scattering factor ($r = -1/2$ for acoustic phonon scattering), carrier concentration (n_H), carrier mobility (μ_H), absolute Seebeck coefficient ($|S|$), electrical resistivity (ρ), total thermal conductivity (κ), and relative density of β-Fe$_{1-x}$Co$_x$Si$_2$ ($0 \leqslant x \leqslant 0.06$) at room temperature.

x	L_O [V^2 K^{-2}]	r	n_H [cm^{-3}]	μ_H [cm^2 V^{-1} s^{-1}]	$|S|$ [μV K^{-1}]	ρ [Ωcm]	κ [W m^{-1} K^{-1}]	Relative density [%]
0	1.792×10^{-8}	$-1/2$	$2.3(2) \times 10^{16}$	37(4)	127	7.10	7.16	98.0(1)
0.005	1.625×10^{-8}	$-1/2$	$9.3(6) \times 10^{18}$	6.1(3)	371	1.08×10^{-1}	8.97	98.5(2)
0.01	1.625×10^{-8}	$-1/2$	$1.84(9) \times 10^{19}$	5.4(2)	357	6.28×10^{-2}	6.72	97.5(1)
0.015	1.627×10^{-8}	$-1/2$	$2.8(4) \times 10^{19}$	5.2(8)	299	4.27×10^{-2}	6.82	97.5(5)
0.02	1.628×10^{-8}	$-1/2$	$1.0(8) \times 10^{20}$	4(2)	287	1.46×10^{-2}	6.30	97.8(2)
0.03	1.644×10^{-8}	$-1/2$	$1.2(4) \times 10^{20}$	3.5(6)	213	1.46×10^{-2}	6.33	97.9(1)
0.04	1.671×10^{-8}	$-1/2$	$1.32(2) \times 10^{20}$	2.47(7)	179	1.92×10^{-2}	5.14	97.9(3)
0.05	1.688×10^{-8}	$-1/2$	$2.5(3) \times 10^{20}$	2.4(4)	167	9.88×10^{-3}	5.18	97.0(5)
0.06	1.735×10^{-8}	$-1/2$	$4.2(8) \times 10^{20}$	1.9(4)	145	7.79×10^{-3}	5.26	96.9(1)

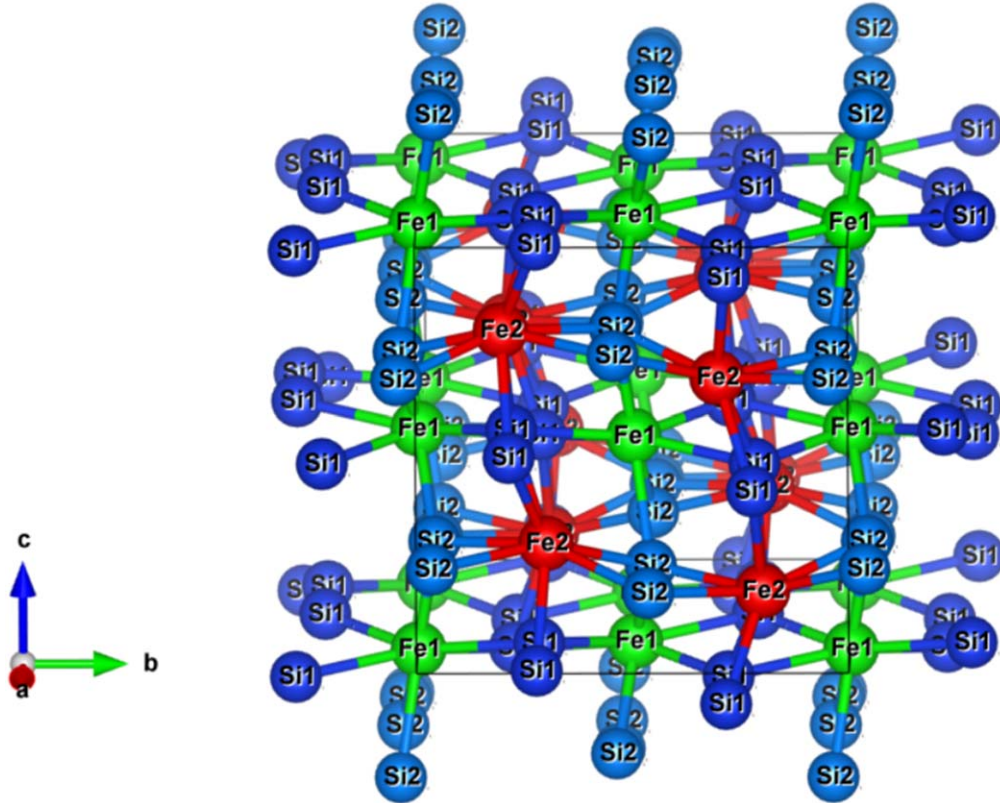**Fig. 3.** (Color online) Crystal structure of β-FeSi$_2$ at room temperature.

$2.3(2) \times 10^{16}$ cm^{-3} and it can be effectively improved to $9.3(0) \times 10^{18} - 4.2(8) \times 10^{20}$ cm^{-3} with Co addition as x increases from 0.005 to 0.06. The relationship between electrical resistivity (ρ) and n_H can be expressed by:

$$\rho = \frac{1}{n_H |e| \, \mu_H}, \qquad (1)$$

where n_H, e, and μ_H are carrier concentration, elementary charge, and carrier mobility, respectively. As a result, for Co-doping samples, the ρ can be effectively decreased due to increasing in n_H. It is considered that Co is the donor to β-FeSi$_2$. In addition, at room temperature, the ρ of $x = 0.00$ and $x = 0.03$ of the current study is about 2 and 1.3 times lower, respectively than those samples fabricated by the cold pressing, sintering, and annealing process reported by Tani and Kido[34] due to the larger μ_H. In addition, the ρ of $x = 0.005$ and $x = 0.06$ of our results is also significantly 18

and 35 times lower, respectively than those samples fabricated by the horizontal chemical vapor transport method reported by Brehme et al.[35] due to the higher n_H. For $x = 0.02$, the n_H of the current study is significantly 10 times higher than that of the sample fabricated by mechanical alloying, hot pressing, and annealing for almost 100 h reported by Ur and Kim,[36] resulting in the decrease in ρ. This suggests that the optimum n_H and μ_H at room temperature to achieve the minimum ρ can be obtained by the sample prepared by arc melting and directly followed by the annealing process, which is relevant for TE application.

At room temperature, the addition of Co causes the reduction in mobility(μ_H) of β-FeSi$_2$ from 37(4) to 1.9(4) cm^2 V^{-1} s^{-1}. As a result, the $|S|$ of $0.005 \leqslant x \leqslant 0.06$ samples are in the range from 371 to 145 μV K^{-1} which is higher than 127 μV K^{-1} of $x = 0$ samples. The relationship of μ_H, n_H, and S can be explained in terms of effective mass m^* by

Table II. Crystal structure parameters of β-Fe$_{1-x}$Co$_x$Si$_2$ ($0 \leqslant x \leqslant 0.10$) at room temperature.

Samples		Fe$_{1-x}$Co$_x$Si$_2$												
Composition, x		0	0.005	0.01	0.015	0.02	0.03	0.04	0.05	0.06	0.07	0.08	0.09	0.1
Space group		*Cmce*	*Cmce*	*Cmce*	*Cmce*	*Cmce*	*Cmce*	*Cmce*	*Cmce*	*Cmce*	*Cmce*	*Cmce*	*Cmce*	*Cmce*
a (Å)		9.8788(5)	9.8792(6)	9.8831(5)	9.8828(5)	9.8833(6)	9.8864(6)	9.8929(5)	9.8962(5)	9.9000(5)	9.892(1)	9.897(1)	9.900(2)	9.917(4)
b (Å)		7.8008(4)	7.8011(4)	7.8032(4)	7.8003(4)	7.8015(5)	7.8003(5)	7.8019(4)	7.8019(4)	7.8021(4)	7.823(1)	7.8205(9)	7.830(1)	7.895(4)
c (Å)		7.8372(4)	7.8361(5)	7.8371(5)	7.8368(4)	7.8347(5)	7.8344(5)	7.8371(4)	7.8371(5)	7.8375(4)	7.792(1)	7.7947(9)	7.793(1)	7.786(4)
V (Å^3)		603.96(5)	603.92(6)	604.40(6)	604.13(5)	604.10(7)	604.16(7)	604.90(6)	605.10(6)	605.38(5)	603.0(1)	603.3(1)	604.2(2)	609.7(5)
Fe1	x	0.2160(2)	0.2165(3)	0.2165(3)	0.2165(2)	0.2167(3)	0.2168(3)	0.2174(3)	0.2177(3)	0.2175(3)	0.2169(7)	0.2168(5)	0.216(1)	0.215(1)
	y	0	0	0	0	0	0	0	0	0	0	0	0	0
	z	0	0	0	0	0	0	0	0	0	0	0	0	0
	B (Å^2)	0.1	0.1	0.1	0.1	0.1	0.1	0.1	0.1	0.1	0.1	0.1	0.1	0.1
	g	1.000	0.995	0.990	0.985	0.980	0.970	0.960	0.950	0.940	0.930	0.920	0.910	0.900
Co1	x	—	0.2165(3)	0.2165(3)	0.2165(2)	0.2167(3)	0.2168(3)	0.2174(3)	0.2177(3)	0.2175(3)	0.2169(7)	0.2168(5)	0.216(1)	0.215(1)
	y	—	0	0	0	0	0	0	0	0	0	0	0	0
	z	—	0	0	0	0	0	0	0	0	0	0	0	0
	B (Å^2)	—	0.1	0.1	0.1	0.1	0.1	0.1	0.1	0.1	0.1	0.1	0.1	0.1
	g	—	0.005	0.010	0.015	0.020	0.030	0.040	0.050	0.060	0.070	0.080	0.090	0.100
Fe2	x	1/2	1/2	1/2	1/2	1/2	1/2	1/2	1/2	1/2	1/2	1/2	1/2	1/2
	y	0.3014(4)	0.3016(4)	0.3019(4)	0.3012(4)	0.2999(4)	0.3017(5)	0.3005(4)	0.3008(5)	0.3010(4)	0.298(1)	0.300(1)	0.282(1)	0.291(3)
	z	0.1940(4)	0.1946(4)	0.1941(4)	0.1935(4)	0.1954(4)	0.1949(4)	0.1948(4)	0.1949(4)	0.1954(4)	0.192(1)	0.1937(9)	0.190(1)	0.120(1)
	B (Å^2)	0.1	0.1	0.1	0.1	0.1	0.1	0.1	0.1	0.1	0.1	0.1	0.1	0.1
	g	1.000	0.995	0.990	0.985	0.980	0.970	0.960	0.950	0.940	0.930	0.920	0.910	0.900
Co2	x	—	1/2	1/2	1/2	1/2	1/2	1/2	1/2	1/2	1/2	1/2	1/2	1/2
	y	—	0.3016(4)	0.3019(4)	0.3012(4)	0.2999(4)	0.3017(5)	0.3005(4)	0.3008(5)	0.3010(4)	0.298(1)	0.300(1)	0.282(1)	0.291(3)
	z	—	0.1946(4)	0.1941(4)	0.1935(4)	0.1954(4)	0.1949(4)	0.1948(4)	0.1949(4)	0.1954(4)	0.192(1)	0.1937(9)	0.190(1)	0.120(1)
	B (Å^2)	—	0.1	0.1	0.1	0.1	0.1	0.1	0.1	0.1	0.1	0.1	0.1	0.1
	g	—	0.005	0.010	0.015	0.020	0.030	0.040	0.050	0.060	0.070	0.080	0.090	0.100
Si1	x	0.1217(5)	0.1218(7)	0.1229(7)	0.1220(6)	0.1225(7)	0.1239(7)	0.1235(7)	0.1236(7)	0.1243(6)	0.119(2)	0.122(1)	0.114(1)	0.118(1)
	y	0.2811(7)	0.2803(8)	0.2806(8)	0.2805(7)	0.2810(8)	0.2807(8)	0.2812(8)	0.2802(8)	0.2812(8)	0.284(1)	0.281(1)	0.287(1)	0.315(4)
	z	0.0394(4)	0.0385(5)	0.0361(5)	0.0389(5)	0.0374(5)	0.0367(5)	0.0371(5)	0.0380(5)	0.0390(5)	0.052(1)	0.047(1)	0.057(1)	0.118(3)
	B (Å^2)	0.3	0.3	0.3	0.3	0.3	0.3	0.3	0.3	0.3	0.3	0.3	0.3	0.3
	g	1.0	1.0	1.0	1.0	1.0	1.0	1.0	1.0	1.0	1.0	1.0	1.0	1.0
Si2	x	0.3761(5)	0.3757(9)	0.3749(6)	0.3744(6)	0.3744(7)	0.3749(7)	0.3745(7)	0.3741(7)	0.3733(6)	0.391(1)	0.389(1)	0.394(1)	0.409(1)
	y	0.0399(5)	0.0395(6)	0.0382(6)	0.0398(5)	0.0397(6)	0.0380(6)	0.0382(6)	0.0397(6)	0.0388(6)	0.047(1)	0.040(1)	0.067(1)	0.074(3)
	z	0.2220(6)	0.2211(7)	0.2215(7)	0.2221(7)	0.2207(7)	0.2223(8)	0.2221(7)	0.2221(7)	0.2225(7)	0.200(1)	0.202(1)	0.192(1)	0.130(3)
	B (Å^2)	0.3	0.3	0.3	0.3	0.3	0.3	0.3	0.3	0.3	0.3	0.3	0.3	0.3
	g	1.0	1.0	1.0	1.0	1.0	1.0	1.0	1.0	1.0	1.0	1.0	1.0	1.0
R_{wp} (%)		3.316	3.609	3.333	3.421	3.473	3.474	3.304	3.236	3.083	5.12	4.512	5.918	6.16
R_P (%)		2.108	2.447	2.183	2.339	2.279	2.309	2.223	2.173	2.092	2.992	2.797	3.531	3.724
R_R (%)		29.041	33.870	33.327	32.334	33.153	34.348	33.803	34.601	33.313	53.27	48.707	62.728	61.415
R_e (%)		0.792	0.772	0.833	0.759	0.767	0.784	0.776	0.763	0.765	0.794	0.728	0.724	0.747
R_B (%)		8.543	9.084	10.441	8.477	9.085	10.058	9.514	9.878	9.467	25.637	17.697	33.123	10.669
R_F (%)		8.603	8.411	9.299	8.553	9.255	8.977	8.532	8.712	8.186	15.789	13.201	18.579	4.666
$S = R_{wp}/R_e$		4.187	4.675	4.001	4.507	4.528	4.431	4.258	4.241	4.030	6.448	6.198	8.174	8.246
Si1–Fe1/Co1 (Å)		2.361(5)	2.361(6)	2.351(6)	2.359(6)	2.350(6)	2.342(6)	2.339(6)	2.343(6)	2.335(6)	2.37(1)	2.36(1)	2.40(1)	2.38(2)

Table II. Continued.

| Samples	Fe$_{1-x}$Co$_x$Si$_2$												
Composition, x	0	0.005	0.01	0.015	0.02	0.03	0.04	0.05	0.06	0.07	0.08	0.09	0.1
Space group	Cmce	Cmce	Cmce	Cmce	Cmce	Cmce	Cmce	Cmce	Cmce	Cmce	Cmce	Cmce	Cmce
Si1–Fe1/Co1 (Å)	2.402(6)	2.397(7)	2.394(7)	2.398(6)	2.400(7)	2.392(7)	2.400(7)	2.395(7)	2.400(7)	2.45(1)	2.42(1)	2.50(1)	2.82(3)
Si1–Fe2/Co2 (Å)	2.282(5)	2.279(6)	2.268(6)	2.276(6)	2.279(7)	2.282(7)	2.282(6)	2.287(5)	2.303(6)	2.31(1)	2.33(1)	2.26(1)	2.35(2)
Si1–Fe2/Co2 (Å)	2.415(4)	2.418(5)	2.443(5)	2.424(5)	2.422(5)	2.438(5)	2.434(5)	2.429(5)	2.422(5)	2.33(1)	2.34(1)	2.30(1)	2.36(2)
Fe1/Co1–Si1–Fe1/Co1 (deg.)	112.3(2)	112.4(2)	113.0(2)	112.4(2)	112.7(2)	113.2(3)	113.0(2)	113.0(2)	113.1(2)	110.4(4)	111.7(4)	107.9(6)	100.2(6)
Fe2/Co2–Si1–Fe2/Co2 (deg.)	116.6(2)	116.6(2)	116.1(2)	116.5(2)	116.2(2)	115.7(2)	115.8(2)	115.8(2)	115.5(2)	117.0(4)	116.0(4)	118.4(7)	113.7(7)
Si2–Fe1/Co1 (Å)	2.372(5)	2.361(6)	2.356(6)	2.358(6)	2.349(6)	2.359(7)	2.352(6)	2.350(7)	2.347(6)	2.35(1)	2.34(1)	2.37(1)	2.25(2)
Si2–Fe1/Co1 (Å)	2.381(5)	2.387(6)	2.380(6)	2.376(6)	2.386(6)	2.375(6)	2.378(6)	2.380(6)	2.373(6)	2.59(1)	2.56(1)	2.69(1)	2.25(2)
Si2–Fe2/Co2 (Å)	2.322(6)	2.321(7)	2.316(7)	2.332(7)	2.339(8)	2.312(8)	2.324(7)	2.333(6)	2.329(7)	2.23(1)	2.30(1)	1.97(1)	1.93(3)
Si2–Fe2/Co2 (Å)	2.388(5)	2.393(6)	2.410(6)	2.397(6)	2.387(6)	2.409(6)	2.403(6)	2.397(6)	2.408(6)	2.38(1)	2.31(1)	2.62(1)	3.09(3)
Fe1/Co1–Si2–Fe1/Co1 (deg.)	113.5(2)	113.6(2)	114.0(2)	114.1(2)	114.0(2)	114.0(2)	114.1(2)	114.1(2)	114.5(2)	105.8(4)	106.9(3)	102.2(5)	91.4(7)
Fe2/Co2–Si2– Fe2/Co2 (deg.)	116.1(2)	115.8(2)	115.5(2)	115.4(2)	115.3(2)	115.5(2)	115.3(2)	115.2(2)	114.8(2)	120.6(5)	119.9(3)	121.1(7)	121.9(7)
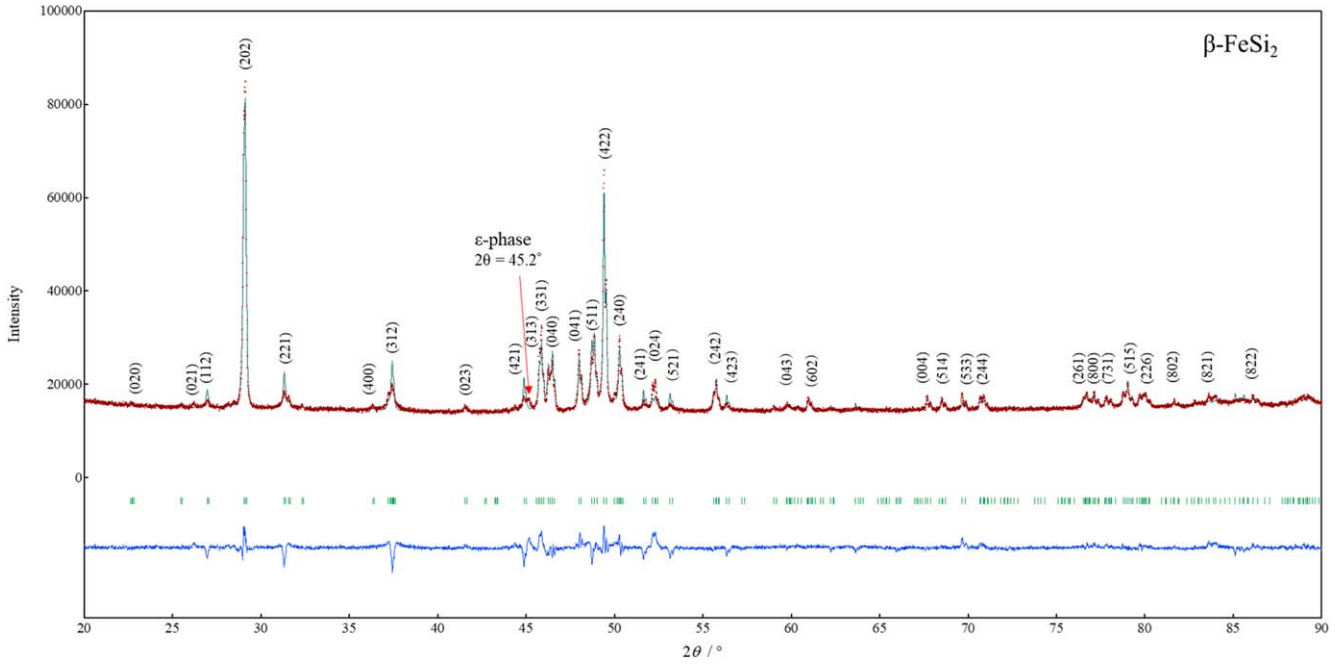
Fig. 4. (Color online) Rietveld analysis of β-FeSi$_2$, where the indexed peaks are the peaks of β-phase.

using the Mott formula[37] as shown in Eqs. (2) and (3):

$$S = \frac{k_B^2 T}{3|e|} \frac{m^*}{\hbar^2} \left(\frac{\pi}{3n_H}\right)^{2/3} \qquad (2)$$

$$m^* = \frac{e\tau}{\mu_H}. \qquad (3)$$

From both Eqs. (2) and (3), the S is proportional to m^*, but m^* has an inverse relationship with μ_H. Therefore, S is also inversely proportional to μ_H. In other words, when the mobility becomes lower, the S becomes higher. The $|S|$ increases with decreasing μ_H only from $x = 0$ to $x = 0.005$ because it is close to the intrinsic semiconductor region with low carrier density where the compensation effect dominates, while for $0.01 \leqslant x \leqslant 0.06$, $|S|$ decreases despite decreasing μ_H because of increasing n_H. Moreover, considering the tendency of $|S|$ in Co-doped samples, the values decrease from 371 to 145 μV K^{-1} as x increases from 0.005 to 0.06, respectively. This kind of tendency can be also explained by Eq. (2), where $|S|$ is inversely proportional to n_H. As shown in Table I or the inset figure of Fig. 6, n_H increases with x, suggesting the reduction in the $|S|$. Moreover, the lowest total thermal conductivity κ_{total} was obtained in $x = 0.04$.

The electrical resistivity (ρ) of non-doped β-FeSi$_2$ drastically decreases from 7.10 to 0.075 Ωcm as temperature increases from 300 to 800 K, respectively as shown in Fig. 6. For Co-doping samples, the ρ significantly decreases as increasing addition amount of Co, where the minimum values are lower than 10^{-2} Ωcm obtained from $x = 0.06$. This is considered that the reduction of ρ can be productively achieved by doping with an impurity having different valence electrons like Co and the n_H can be consequently increased as shown in the inset of Fig. 6, indicating that Co is the donor to β-FeSi$_2$. More interestingly, compared to a non-doped sample, the ρ of each Co-doping sample is approximately stable over the measured temperature range. It is probably because the ionized impurity-electrons scattering process is stable or independent of temperature. The carrier concentration and mobility of Co-doped samples are probably independent of temperature. This remarkable reduction of ρ with stability leads to a significantly enhanced power factor (PF) of the TE material.

The Seebeck coefficient of both non-doped and Co-doped β-FeSi$_2$ samples shows negative values indicating that they are all n-type semiconducting materials as shown in Fig. 7. The absolute Seebeck coefficient $|S|$ of non-doped β-FeSi$_2$ remarkably increases from about 120–290 μV K^{-1} at the temperature from 300 to 420 K, respectively, and it then turns to decrease to around 0 μV K^{-1} when the temperature reaches 800 K due to the bipolar effect. This bipolar effect is effectively reduced by Co-doping owing to the increase in n_H from $2.3(3) \times 10^{16}$ to $4.2(8) \times 10^{20}$ cm^{-3} at $0 \leqslant x \leqslant 0.06$, respectively. The result of the current study is in agreement with that of Gong et al. when the n_H of CaMg$_2$Bi$_2$ system was increased from 1.0×10^{16} to 1.0×10^{22} cm^{-3}, the bipolar effect can be improved resulting in the stability of $|S|$ at high temperature.[20] The $|S|$ of all Co-doped samples is higher than that of the non-doped sample due to the decrease in Hall mobility as shown in Table I or the inset of Fig. 7. However, the $|S|$ decreases with increasing Co addition due to the increase in n_H as shown in the inset of Fig. 6.

Figure 8 shows the power factors (PF) of all samples. The PF is calculated by PF $= S^2/\rho$. As shown in the inset of Fig. 8, the highest PF of non-doped β-FeSi$_2$ is around 3.4 μWm^{-1}K^{-2} at 450 K which is quite low compared to that of Co-doped β-FeSi$_2$. By doping with Co, the PF is significantly enhanced, where the optimum doping level $x = 0.03$ with the maximum value of around 900 μWm^{-1}K^{-2} at the temperature range from 720 to 800 K. The enhancement of PF can be achieved by the elimination of the bipolar effect by increasing n_H; therefore, the electrical conductivity and Seebeck coefficient can be simultaneously improved. However, the PF turns to decrease from that level ($x = 0.03$) even if we try with a higher doping level from
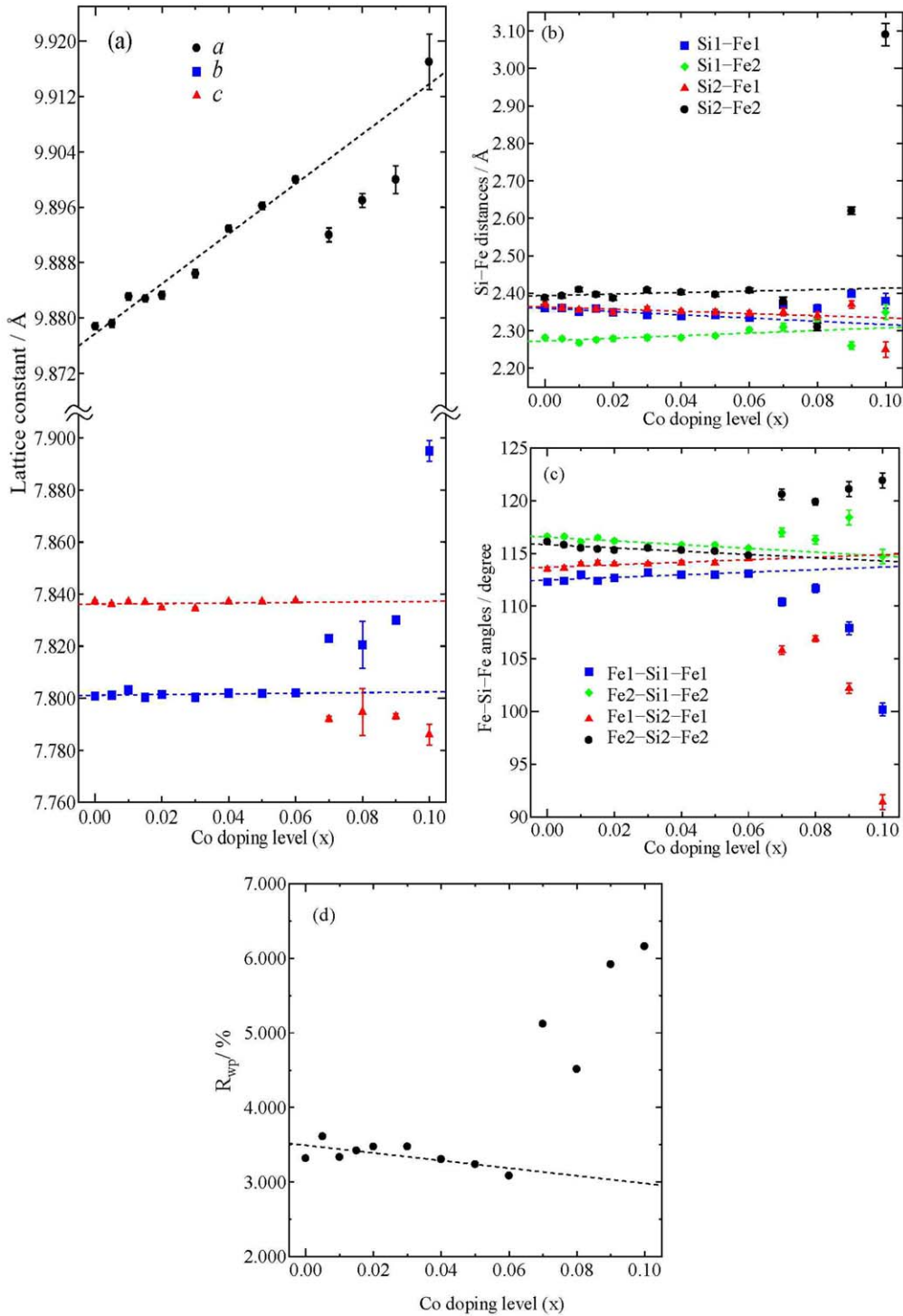
Fig. 5.   (Color online) (a) Lattice constants (b) Si–Fe distances, (c) Fe–Si–Fe angles, and (d) R_{wp} of β-Fe$_{1-x}$Co$_x$Si$_2$ ($0 \leqslant x \leqslant 0.10$) at room temperature.

$x \geqslant 0.04$ due to the reduction values of $|S|$ with higher Co-doping resulting from the increase in n_H.

The total thermal conductivity κ of all Co-doping samples ($0.005 \leqslant x \leqslant 0.06$) seems to be fluctuated in the range from about 5–9 W m^{-1} K^{-1} around that of a non-doped sample as can be seen in Fig. 9. The high values of κ are found in $x = 0.005$, while the minimum values of that are obtained in $x = 0.04$. In addition, the electronic thermal (κ_e) conductivity of the β-Fe$_{1-x}$Co$_x$Si$_2$ system is calculated from $L_O T/\rho$, where L_O is the Lorenz number calculated from the Seebeck coefficient of each sample at room temperature as shown in Table I. In addition, the Lorenz number of all samples

($0 \leqslant x \leqslant 0.06$) is calculated by using scattering factor $r = -1/2$ (acoustic phonon scattering). The relationship of L_O in terms of r can be expressed by:

$$L_O = \left(\frac{k_B}{e}\right)^2 \left[\frac{\left(r + \frac{7}{2}\right)F_{r+\frac{5}{2}}(\eta)}{\left(r + \frac{3}{2}\right)F_{r+\frac{1}{2}}(\eta)} - \left\{ \frac{\left(r + \frac{5}{2}\right)F_{r+\frac{3}{2}}(\eta)}{\left(r + \frac{3}{2}\right)F_{r+\frac{1}{2}}(\eta)} \right\}^2 \right],$$

(4)

where the function is given as: $F_n(\eta) = \int_0^\infty \frac{\chi^n}{1 + e^{\chi - \eta}}d\chi$, $\chi = \frac{E}{k_B T}$, $\eta = \frac{E_F}{k_B T}$ and E_F is Fermi energy.
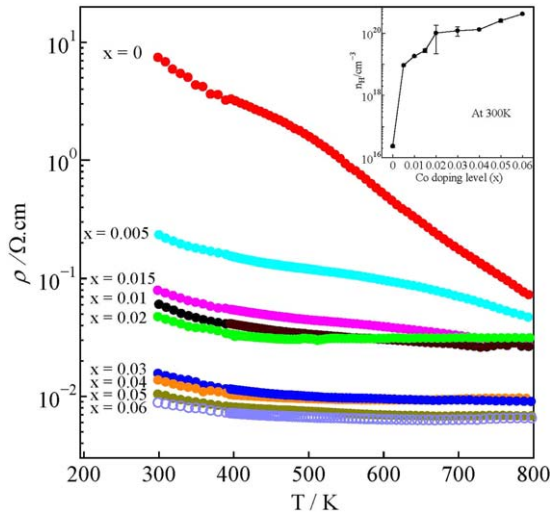
Fig. 6. (Color online) Temperature dependence of electrical resistivity of β-Fe$_{1-x}$Co$_x$Si$_2$ ($0 \leqslant x \leqslant 0.06$), where the carrier concentration, n_{H}, is plotted with $0 \leqslant x \leqslant 0.06$ as shown in the inset.
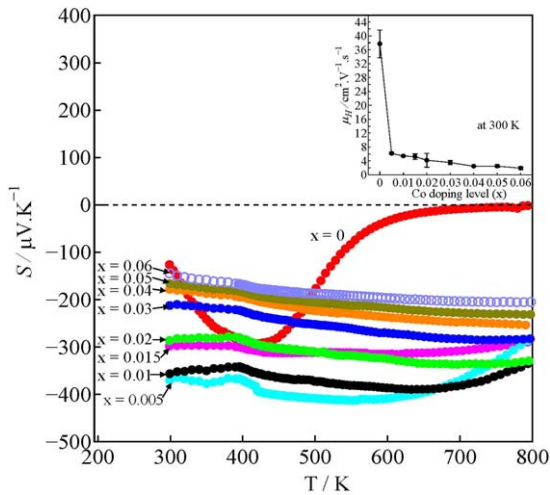

Fig. 7. (Color online) Temperature dependence of Seebeck coefficient of β-Fe$_{1-x}$Co$_x$Si$_2$ ($0 \leqslant x \leqslant 0.06$), where the carrier mobility, μ_{H}, is plotted with $0 \leqslant x \leqslant 0.06$ as shown in the inset.
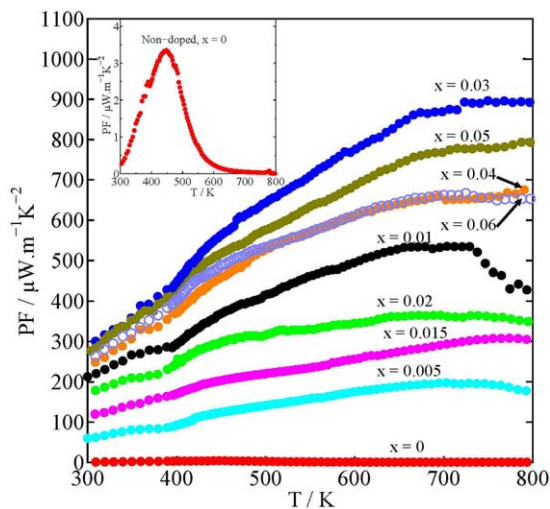
Fig. 8. (Color online) Temperature dependence of power factor (PF) of β-Fe$_{1-x}$Co$_x$Si$_2$ ($0 \leqslant x \leqslant 0.06$), where the PF of a non-doped sample ($x = 0$) is magnified as shown in the inset.
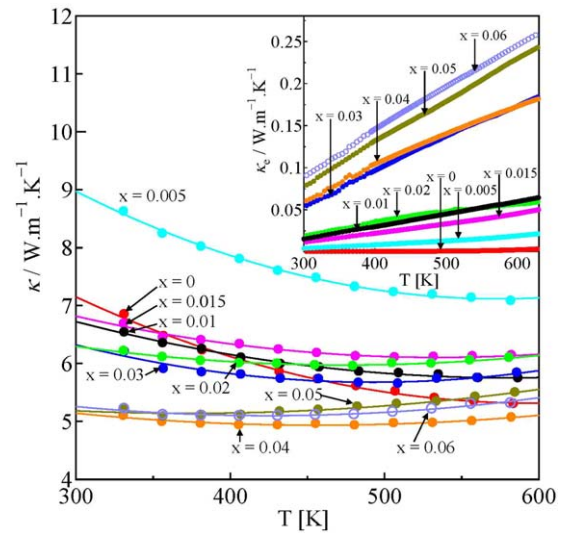
Fig. 9. (Color online) Temperature dependence of total thermal conductivity ($\kappa = \kappa_{\mathrm{L}} + \kappa_{\mathrm{e}}$) of β-Fe$_{1-x}Co_xSi_2$ ($0 \leqslant x \leqslant 0.06$), where $\kappa_{\mathrm{e}} = L_{\mathrm{o}}T/\rho$ is calculated by Wiedemann–Franz law and plotted in the inset.

As can be seen in Table I, in Co-doping samples, as x increases from 0.005 to 0.06, the Lorenz number increases with decreasing $|S|$, indicating the phase transition from semiconducting β-phase to metallic α-phase, which can be proved by XRD patterns as shown in Fig. 1. The κ_{e} increase with increasing x over the measured temperature due to the decrease in ρ; however, its values are very low and can be neglected as shown in the inset of Fig. 9. Therefore, the lattice thermal conductivity (κ_{L}) dominates the total thermal conductivity (κ).

Figure 10 shows the temperature dependence of ZT of β-Fe$_{1-x}$Co$_x$Si$_2$ ($0 \leqslant x \leqslant 0.06$). As can be seen in the inset of Fig. 10, the highest ZT of non-doped β-FeSi$_2$ ($x = 0$) is around 2.6×10^{-4} at 450 K which is very low compared to that of Co-doped β-FeSi$_2$. The same as the power factor, the enhancement of ZT can be obtained with Co-doping, where the optimum doping level $x = 0.03$ with its highest value of about 0.099 at the temperature range from 720 to 800 K. The
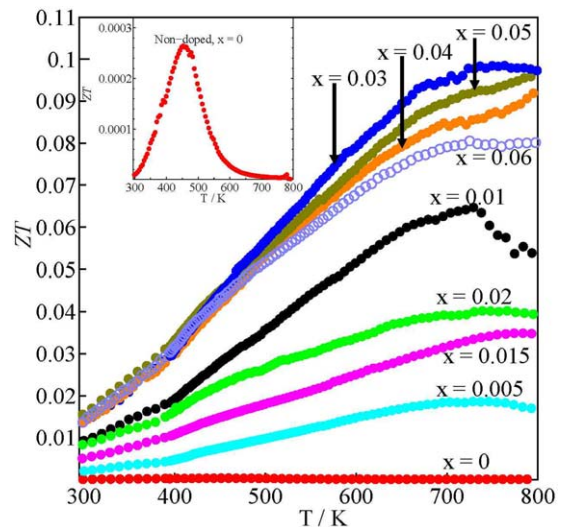

Fig. 10. (Color online) Temperature dependence of ZT of β-Fe$_{1-x}$Co$_x$Si2 ($0 \leqslant x \leqslant 0.06$), where the ZT of the non-doped sample ($x = 0$) is magnified as shown in the inset.

increase in ZT is due to the absence of the bipolar effect at high n_H while the $|S|$ increases and ρ decreases, resulting in the enhancement of PF, and a slight reduction in κ. On the other hand, the ZT becomes decreasing from that level when doping with higher concentration ($x \geqslant 0.04$) due to the reduction values of $|S|$ caused by the increase in n_H. Therefore, the optimum n_H for maximizing ZT is around $1.2(4) \times 10^{20}$ cm^{-3} obtained in $x = 0.03$ sample.

4. Conclusions

β-Fe$_{1-x}$Co$_x$Si$_2$ ($0 \leqslant x \leqslant 0.10$) samples were successfully fabricated and the presence of a small amount of ε-phase appeared in all samples, but α-phase only appeared in $0.07 \leqslant x \leqslant 0.10$ samples. Since the presence of metallic α-phase provokes the low TE performance due to the decrease in the Seebeck coefficient, the measurement of TE properties was only performed in $0 \leqslant x \leqslant 0.06$ samples. The thermoelectric properties such as electrical resistivity (ρ), Seebeck coefficient (S), and thermal conductivity (κ) were measured at the temperature range from 300 to 800 K. In addition, the measurement of carrier concentration (n_H) and Hall mobility (μ_H) was performed at room temperature. The ρ decreases with increasing x from 0 to 0.06 due to the increase in n_H from $2.3(2) \times 10^{16}$ to $4.2(8) \times 10^{20}$ cm^{-3}, respectively. The $|S|$ of all Co-doped samples ($0.005 \leqslant x \leqslant 0.06$) are more stable over measured temperature than that of $x = 0$ due to a reduction in bipolar effect where the μ_H remarkably reduces from 37(4) to 1.9(4) cm^2 V^{-1} s^{-1}. The power factor (PF) is consequently improved with Co-doping; however, the optimum point is obtained in $x = 0.03$ with the highest value around 900 μWm^{-1}K^{-2} at the temperature range from 720 to 800 K. The thermal conductivity (κ) slightly decreases with Co addition, where the lowest κ_{total} is found in $x = 0.04$ over the measured temperature. As a result, the highest $ZT = 0.099$ at the temperature range from 720 to 800 K is obtained in $x = 0.03$ with the optimum carrier concentration around $1.2(4) \times 10^{20}$ cm^{-3}. In this study, almost the same thermoelectric properties are obtained by comparing to the pressure sintering samples reported by Kim et al.,[25] but it is lower than that of the spark plasma sintering (SPS) samples reported by Tani and Kido.[24] Thus, it is a future task to minimize the thermal conductivity of polycrystalline β-FeSi$_2$ samples.

1) F. Fitriani, R. Ovik, B. D. Long, M. C. Barma, M. Riaz, M. F. M. Sabri, S. M. Said, and R. Saidur, Renew. Sust. Energ. Rev. **64**, 635 (2016).
2) M. H. Elsheikh, D. A. Shnawah, M. F. MohdSabri, S. B. MohdSaid, M. H. Hassan, M. B. A. Bashir, and M. Mohamad, Renew. Sust. Energ. Rev. **30**, 337 (2014).
3) G. Q. Shu, Y. C. Liang, H. Q. Wei, H. Tian, J. Zhao, and L. N. Liu, Renew. Sust. Energ. Rev. **19**, 385 (2013).
4) M. Ito, T. Tanaka, and S. Hara, J. Appl. Phys. **95**, 6209 (2004).
5) X. F. Zheng, C. X. Liu, Y. Y. Yan, and Q. Wang, Renew. Sust. Energ. Rev. **32**, 486 (2014).
6) T. Watanabe, M. Hasaka, T. Morimura, and H. Nakashima, J. Alloys Compd. **417**, 241 (2006).
7) A. Nozariasbmarz et al., Jpn. J. Appl. Phys. **56**, 05DA04 (2017).
8) A. T. Burkov, Phys. Status Solidi A **215**, 1800105 (2018).
9) E. Arushanov and K. G. Lisunov, Jpn. J. Appl. Phys. **54**, 07JA02 (2015).
10) X. L. Du, P. Qiu, J. Chai, T. Mao, P. Hu, J. Yang, Y. Sun, X. Shi, and L. Chen, ACS Appl. Mater. Interfaces **12**, 12901 (2020).
11) F. Dabrowski, L. Ciupinski, J. Zdunek, J. Krsuzewski, R. Zybala, A. Michalski, and K. J. Kurzydloski, Mater. Today: Proc. **8**, 531 (2019).
12) W. S. Liu, B. P. Zhang, J. F. Li, H. L. Zhang, and L. D. Zhao, J. Appl. Phys. **102**, 103717 (2007).
13) J. Liu, Q. F. Sun, and X. C. Xie, Phys. Rev. B **81**, 245323 (2010).
14) R. Liu, P. Qiu, X. Chen, X. Huang, and L. Chen, J. Mater. Res. **26**, 1813 (2011).
15) W. Liu, X. Yan, G. Chen, and Z. Ren, Nano Energy. **1**, 42 (2012).
16) H. Fang, T. Feng, H. Yang, X. Ruan, and Y. Wu, Nano Lett. **13**, 2058 (2013).
17) J. He, M. G. Kanatzidis, and V. P. Dravid, Mater. Today **16**, 166 (2013).
18) L. D. Zhao et al., Energy Environ. Sci. **6**, 3346 (2013).
19) J.-H. Bahk and A. Shakouri, Appl. Phys. Lett. **105**, 052106 (2014).
20) J. J. Gong, A. J. Hong, J. Shuai, L. Li, Z. B. Yan, Z. F. Ren, and J.-M. Liu, Phys. Chem. Chem. Phys. **18**, 16566 (2016).
21) Z. W. Chen, X. Zhang, J. Ren, Z. Zeng, Y. Chen, J. He, L. Chen, and Y. Pei, Nat. Commun. **12**, 3837 (2021).
22) S. J. Clark, H. M. Al-Allak, S. Brand, and R. A. Abram, Phys. Rev. B **58**, 16 (1998).
23) M. Ohtaki, D. Ogura, K. Eguchi, and H. Arai, Chem. Lett. **22**, 1067 (1993).
24) J. Tani and H. Kido, Jpn. J. Appl. Phys. **40**, 3236 (2001).
25) S. W. Kim, M. K. Cho, Y. Mishima, and D. C. Choi, Intermetallics **11**, 399 (2003).
26) S-C. Ur, Proc. ICT'03 **22**, 149 (2003).
27) F. Redzuan, I. Mikio, and T. Masatoshi, J. Mater. Sci. **53**, 7683 (2018).
28) S. Le Tonquesse, Z. Verastegui, H. Huynh, V. Dorcet, Q. Guo, V. Demange, C. Prestipino, D. Berthebaud, T. Mori, and M. Pasturel, ACS Appl. Energy Mater. **2**, 8525 (2019).
29) T. Kojima, K. Masumoto, M. A. Okamoto, and I. Nishida, J. Less-Common Met. **159**, 299 (1990).
30) X. Qu, S. Lü, J. Hu, and Q. Meng, J. Alloys Compd. **509**, 10217 (2011).
31) K. Nogi and T. Kita, J. Mater. Sci. **35**, 5845 (2000).
32) F. Dabrowski, L. Ciupinski, J. Zdunek, W. Chrominski, M. Kruszewski, R. Zybala, A. Michalski, and K. J. Kurzydlowski, Arch. Metall. Mater. **66**, 1157 (2021).
33) I. Dezsi, C. Fetzer, M. Kiss, S. Degroote, and A. Vantomme, J. Appl. Phys. **98**, 073523 (2005).
34) J. Tani and H. Kido, J. Appl. Phys. **84**, 1408 (1998).
35) S. Brehme, G. Behr, and A. Heinrich, J. Appl. Phys. **89**, 3798 (2001).
36) S. C. Ur and I. H. Kim, Mater. Lett. **57**, 543 (2002).
37) N. F. Mott, J. Non-Cryst. Solids **1**, 1 (1968).